Structural Gradients Developed in Injection-Molded Syndiotactic Polystyrene (sPS)

Y. ULCER,[1] M. CAKMAK,[1,*] J. MIAO,[2] and C. M. HSIUNG[2]

[1]Polymer Engineering Institute, College of Polymer Engineering and Polymer Science, University of Akron, Akron, OH 44325-0301; [2]University of Southwestern Louisiana, Louisiana Productivity Center, Lafayette, LA 70504-4172

SYNOPSIS

In this experimental research, we investigated the influence of processing history on the development of structural gradients in injection-molded syndiotactic polystyrene (sPS). The structures formed during injection molding of this slow-to-crystallize polymer are explained by the complex interplay between the mechanical history of the sample and the cooling conditions dictated by such variables as mold temperature, cavity geometry, and injection speed. When crystallized under shear, sPS exhibits unusually high preferential chain orientation along the flow direction; this orientation gradually decreases toward the core. The mechanical properties are related to the degree of orientation and crystallinity. © 1996 John Wiley & Sons, Inc.

INTRODUCTION

Syndiotactic polystyrene (sPS) is a recently developed engineering thermoplastic, synthesized using metallocene catalysts.[1,2] Its high heat deflection temperature, high stiffness, good chemical resistance, and low dielectric constant are attractive features for the automotive, appliance, packaging, and electronic industries.[3]

This polymer exhibits complex polymorphic behavior involving three different crystal structures and several mesomeric forms.[1,4-19] The α form,[9] the most common crystal form, was first observed by Ishihara and colleagues, and its detailed structure was determined by Greis and coworkers.[5,6] This form, belonging to the space group $P\bar{6}2c$, is hexagonal with $a = 26.25$ Å, $c = 5.045$ Å, and a crystalline density of $\rho = 1.033$ g/cm^3. The polymer chains in this form are in planar zigzag conformation. The second crystal form, called β,[4,9] is orthorhombic with $a = 8.81$ Å, $b = 28.82$ Å, and $c = 5.08$ Å. The polymer chains in this form are also in planar zigzag conformation. After solvent treatments, Vittoria and colleagues[7,8] obtained a new crystal form in which

the chains attain helical conformation (δ-forms). The unit cell parameters of δ forms depended on the type of solvent. Guerra and coworkers[9] gave a detailed analysis of the conditions leading to different crystal forms of sPS. They also reported that solvent removal from the δ-forms resulted in another crystal form (γ-form) with helical conformation. The γ-form, being apparently metastable, transforms into the α-form upon heat treatment. The formation of the mesomorphic order through mechanical, thermal, and/or solvent treatments of glassy sPS was also reported.[8,10] More recent studies concentrated on the details of the formation and the structure of the polymorphic and mesomorphic forms.[11-19]

Normal vibrational analysis of α-form sPS was carried out by Reynolds and Hsu[20] and that of β-form was done by Nyquist and coworkers.[21] Fourier transform infrared (FTIR) analysis of the polymorphism was also carried by several authors.[22-25] It has been reported that there are bands corresponding to different crystal forms of sPS. Particularly, the band at 1222 cm^{-1} is characteristic of the α-form and that at 935 cm^{-1} is characteristic of the β-form of sPS.

The equilibrium melting point, fusion enthalpy, and fusion entropy of sPS were determined to be 285.5°C,[26] 8.57 kJ/mole, and 15.88 J(K mole),[27] respectively. A special annealing procedure yielding
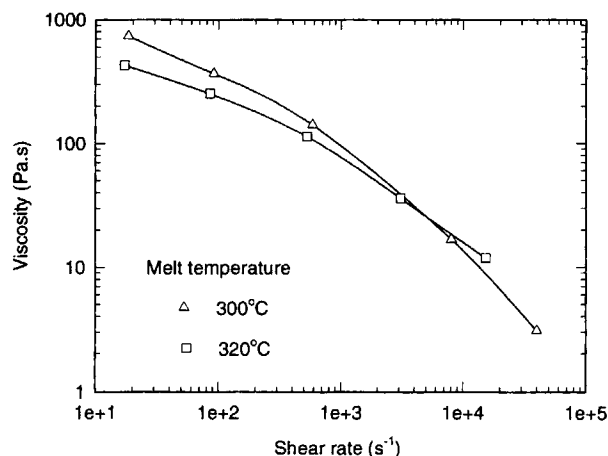

Figure 1   Shear viscosity of sPS as function of shear rate.

sPS with a melting point of 291.5°C (that is, 6°C higher than the calculated equilibrium melting temperature) was reported by Gvozdic and Meier.[28] Studies of crystallization of sPS from the molten[29,30] and glassy[31] states showed that the spherulitic growth rate of sPS is about one order of magnitude higher than isotactic polystyrene (iPS) and that the crystallization half-time has a minimum between 140°C and 200°C. As with iPS, the nucleation density of the sPS increased upon crystallization from the glassy state.

De Candia and colleagues[32] studied the drawing and dynamic mechanical behavior of sPS films in the temperature range 110–200°C. Their results showed that the glass transition temperature (T_g) and crystallinity were affected by drawing and depended strongly on drawing temperature. They reported that at 110°C, films were drawn with the least tension. Hsiung and Cakmak[33] studied the uniaxial free width stretching of amorphous and crystalline sPS films in the temperature range of 100–120°C. They observed that the processability window (i.e., the region between cold crystallization temperature and T_g) narrowed as the stretching ratio increased. They reported 110°C as the optimum processing temperature for the sPS films. Their refractive index measurements and wide-angle X-ray scattering (WAXS) studies indicated that this narrowing was due to increasing stress-induced crystallinity and molecular orientation. Both investigative groups— de Candia and colleagues, and Hsiung and Cakmak—reported the formation of α-form crystals during film processing of sPS.

With the growing industrial use of engineering thermoplastics in the manufacturing of high-performance parts, a number of studies of injection

molding of such polymers have appeared in the recent literature.[34–37] These include slowly crystallizing polycondensates such as poly(phenylene sulfide) (PPS),[34] poly(aryl ketones),[35,36] and poly(ethylene naphthalate (PEN).[37] The common feature of all these polymers is the formation of the amorphous (skin)–semicrystalline (intermediate)–amorphous (core) type of multilayer structures in the thickness direction. The major processing parameters influencing the formation of these structures were found to be the injection speed and mold temperature. At elevated temperatures, where the thermally activated crystallization became significant, these polymers behaved similar to fast-crystallizing polymers such as polyethylene and polypropylene. In this paper we report the effects of injection-molding variables on the structures of injection-molded sPS small dumbbells.

EXPERIMENTAL

Materials

The sPS used in this study was provided by Dow Chemical Co., Midland, MI. The sPS pellets, having
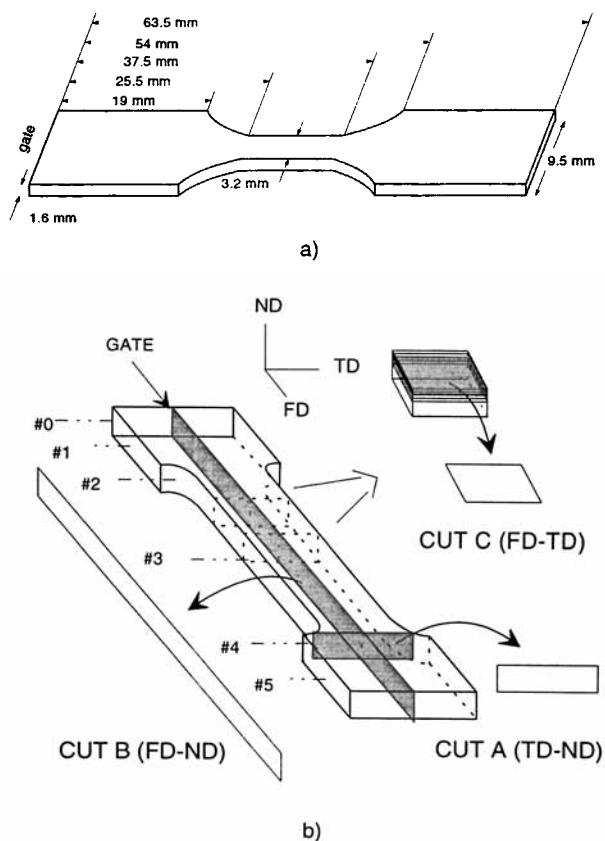

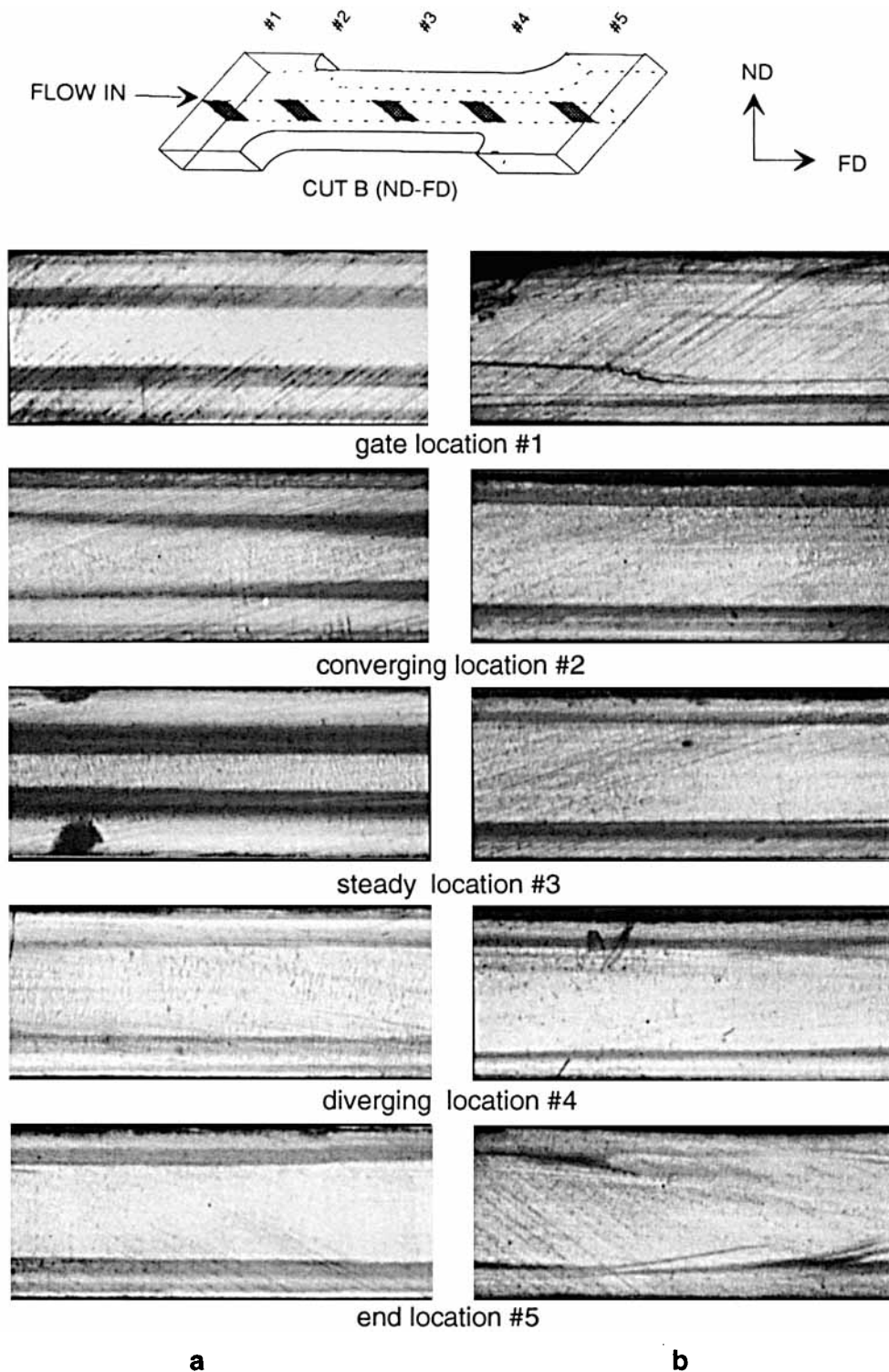**Figure 2**   Dimensions of the cavity and schematics of the cutting procedures.

Figure 3 Transmission photomicrographs of the B-cut samples taken from the indicated locations of the samples molded at 40°C. Injection speed is (a) 6.9 cm³/s; (b) 34.5 cm³/s.

an average molecular weight of $M_w \cong 400{,}000$, were dried in a vacuum oven at 85°C for 12 h before processing. The rheological properties of the material were determined using a Kayeness Glaxy V (model 8052) capillary rheometer. Dies having a diameter of 3.81 mm and length-to-diameter (L/D) ratios of 10, 20, and 30 were used. The experiments were performed at 300°C and 320°C and the results were
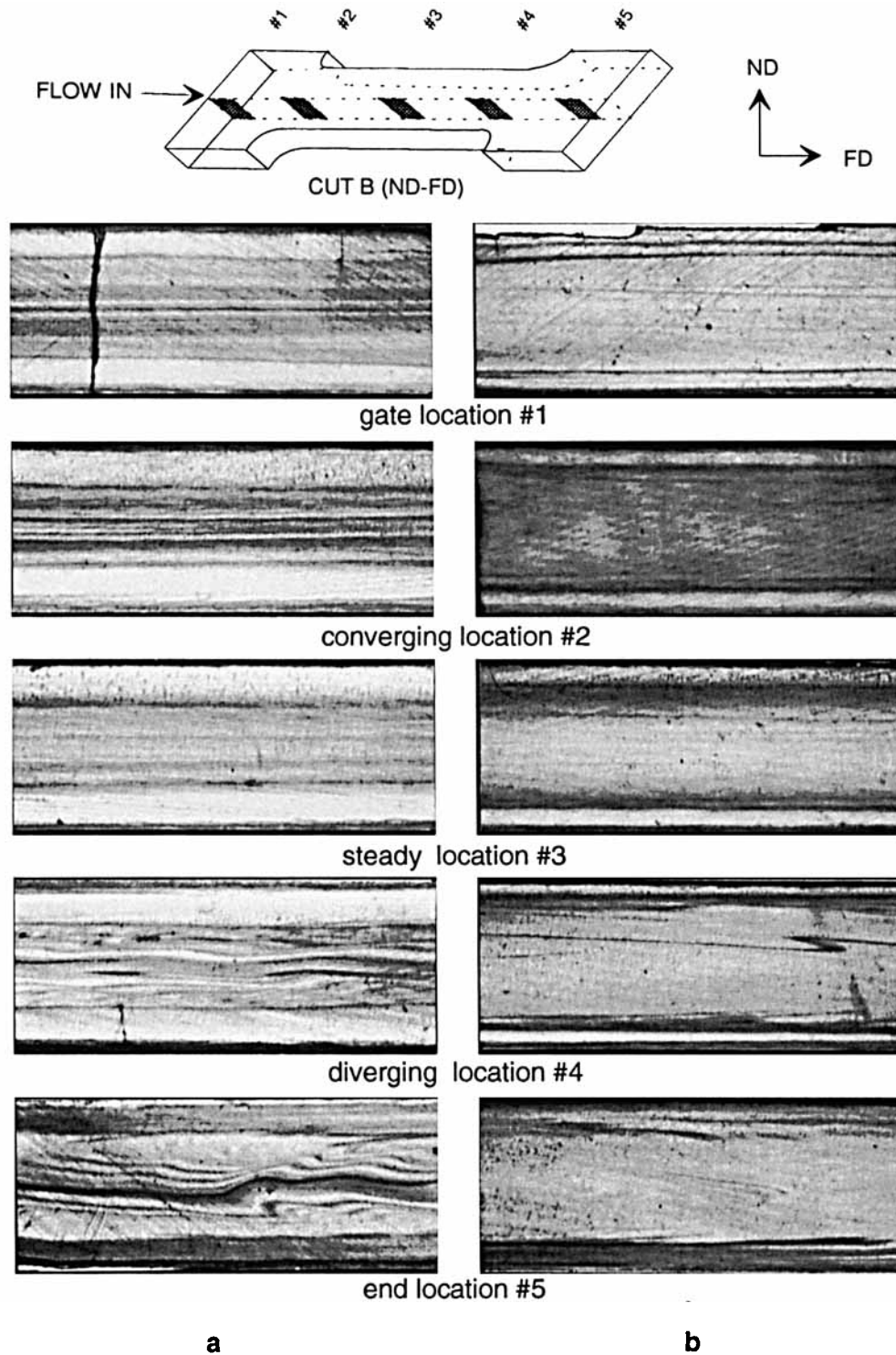
Figure 4 Transmission photomicrographs of the B-cut samples taken from the indicated locations of the samples molded at 110°C. Injection speed is (a) 6.9 cm³/s; (b) 34.5 cm³/s.

corrected for the end effects. Figure 1 represents the shear viscosity as a function of shear stress for sPS. We observed a typical shear thinning effect; however, in the studied shear rate range, the Newtonian plateau was absent.

Injection Molding

End-gated ASTM small dumbbells [Fig. 2(a)] were injection-molded using a Boy 15S injection molding machine at 280°C. Three mold temperatures—40°C,
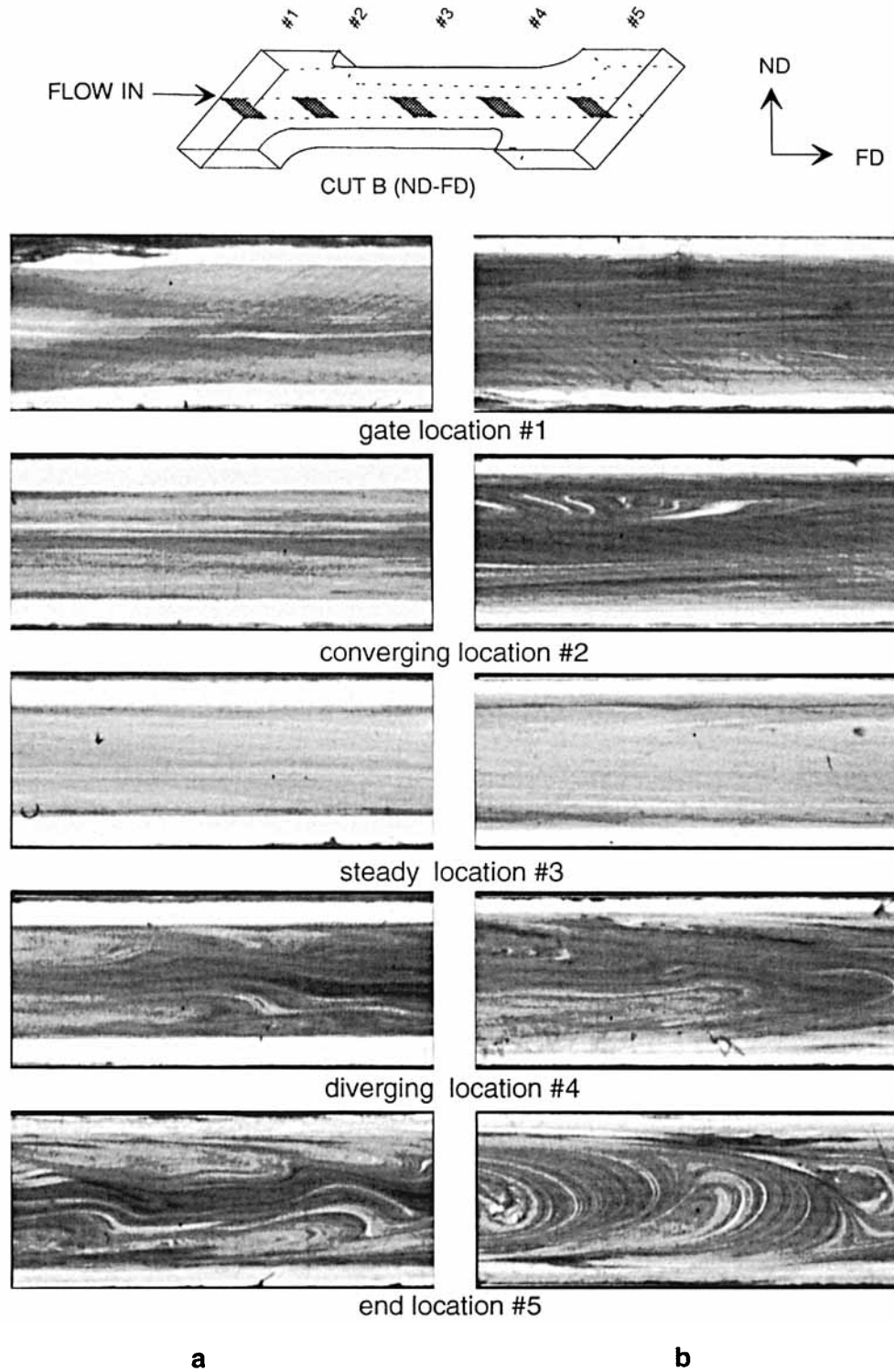
Figure 5 Transmission photomicrographs of the B-cut samples taken from the indicated locations of the samples molded at 140°C. Injection speed is (a) 6.9 cm³/s; (b) 34.5 cm³/s.

110°C, and 140°C—were used. The material was injected using three different injection speeds corresponding to volumetric flow rates of 34.5 cm³/s (high),

6.9 cm³/s (medium), and 2.1 cm³/s (low). The holding time, injection pressure, and back pressure were kept constant at 60 s, 13.8 MPa, and 2.75 MPa, respectively.
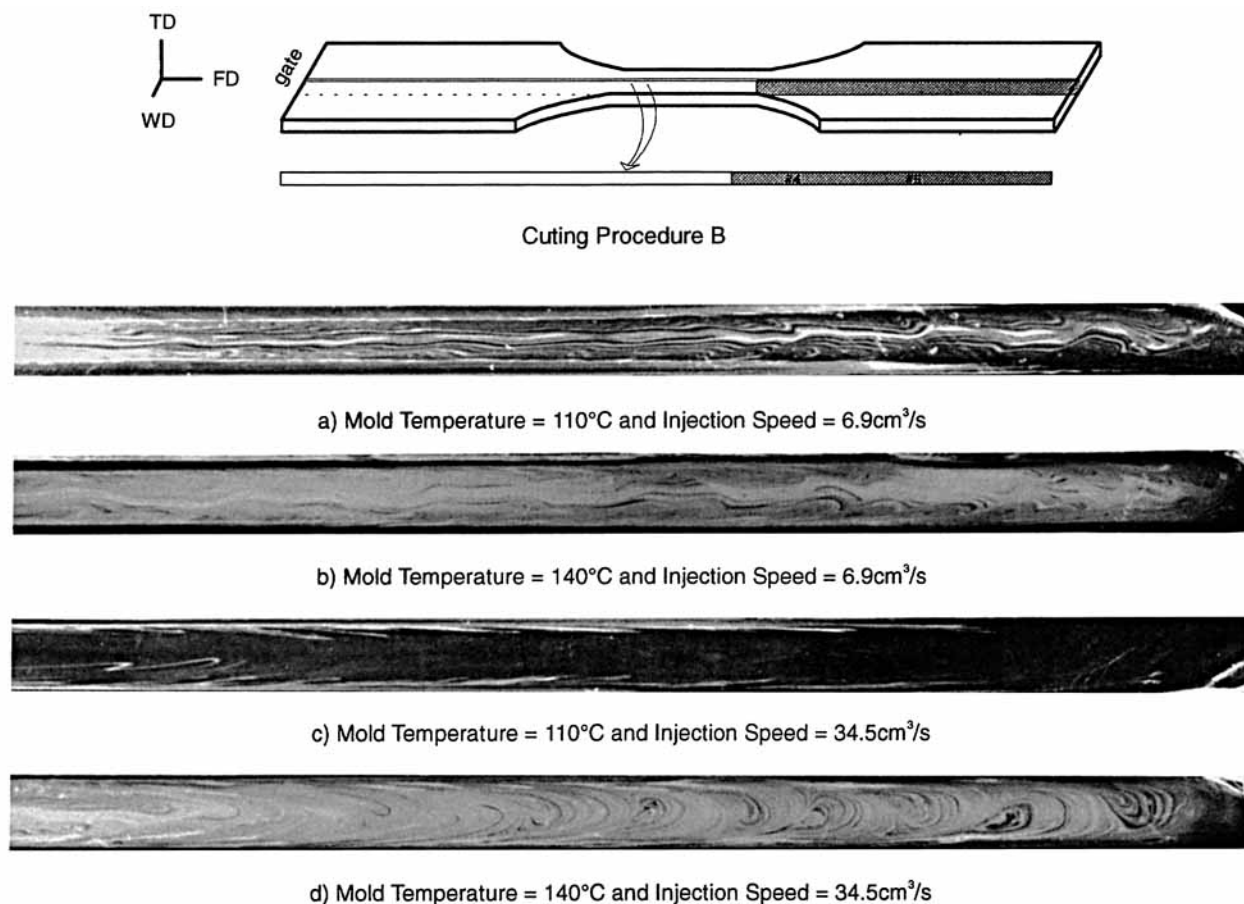
Figure 6 Transmission photomicrographs showing the complex flow patterns at the end of the cavity (the samples were used as negatives). B-cut; injection speed is: (a) and (b), 6.9 cm^3/s; (c) and (d), 34.5 cm^3/s.

Cutting Procedures

Three cutting procedures were used to section the samples [Fig. 2(b)]. Procedure A consisted of cutting sections perpendicular to the flow direction in the TD–ND plane. In procedure B the samples were sectioned parallel to the flow direction in the FD–ND plane, along the center of the sample. Finally, procedure C consisted of cutting sections from skin to core, parallel to flow direction in the FD–TD plane. Samples having an average thickness of 0.4 mm were cut with a Leco Varicut VC-50 diamond saw, and samples having an average thickness of 20 μm were cut using a Reichert-Jung 2050 microtome.

Optical Microscopy

The transmission optical photomicrographs of the cut samples were taken through a Leitz Laborlux 12 POL S microscope using a Nikon 8008S camera. In cases where reproduction of internal structures re-quired high contrast and detail, the samples were used as negatives in the photographic enlarger.

Differential Scanning Calorimetry (DSC)

The thermal analysis of microtomed samples cut with procedure C was carried out in the temperature range 0–300°C using a TA Instruments DSC (model 2910) with a heating rate of 10°C/min. Crystallinity was calculated through

$$X = \frac{\Delta H_{exp}}{\Delta H^\circ} \qquad (1)$$

where $\Delta H_{exp} = \Delta H_{melting} - \Delta H_{cold\ crystallization}$, and $\Delta H^\circ = 53.2$ J/g[27] is the heat of fusion of 100% crystalline sPS.

Hot-Stage Microscopy

A sample microtomed from location #2 of a small dumbbell was placed between thin cover glasses and
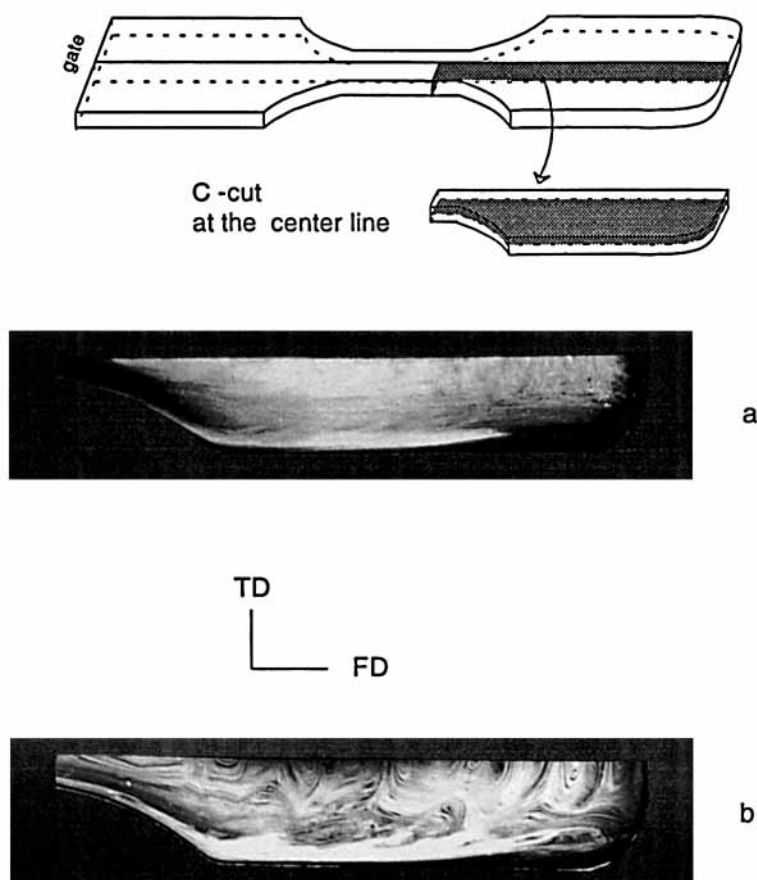
Figure 7 Transmission photomicrographs showing the complex flow patterns at the end of the cavity (the samples were used as negatives). C-cut; mold temperature is 140°C. Injection speed is (a) 6.9 cm³/s; (b) 34.5 cm³/s.

placed in a Mettler FP82 HT hot stage. The hot stage was placed at a 45-degree angle to the extinction axes of the cross-polars of the Leitz microscope. The sample was heated at 10°C/min in the temperature range 50–310°C. The heating and melting event was recorded with a Sony 3 CCD camera connected to both a video recorder and the image-capturing card of a Sun 4/150 workstation.

Fourier Transform Infrared Spectroscopy (FTIR)

Microtomed samples cut from different locations using procedure B were scanned from skin to core on the microscope stage of a Perkin-Elmer model 16C FTIR spectrometer. Samples were scanned 15 times at a 2 cm⁻¹ resolution.

Microbeam Wide Angle X-Ray Diffraction (WAXD)

Skin-to-core WAXD patterns of the B-cuts were taken using the matrixing microbeam X-ray camera

(MMBX) developed in our laboratories.[38] The camera was connected to a Rigaku RU-200B rotating anode X-ray generator operated at 40 kV and 150 mA. The CuKα beam, having a 100-μm diameter, was obtained using a nickel foil monochromatizer and a pinhole collimator.

Tensile Testing

The small dumbbells having an initial gauge length of 19.2 mm were tested using a Q-TEST-6 tensile testing machine at 22°C (room temperature). The drawing rate was 1.27 mm/min. Five samples were tested for each condition and the results were averaged.

RESULTS

Optical Microscopy

Figures 3, 4, and 5 show the unpolarized optical photomicrographs of the samples cut from different
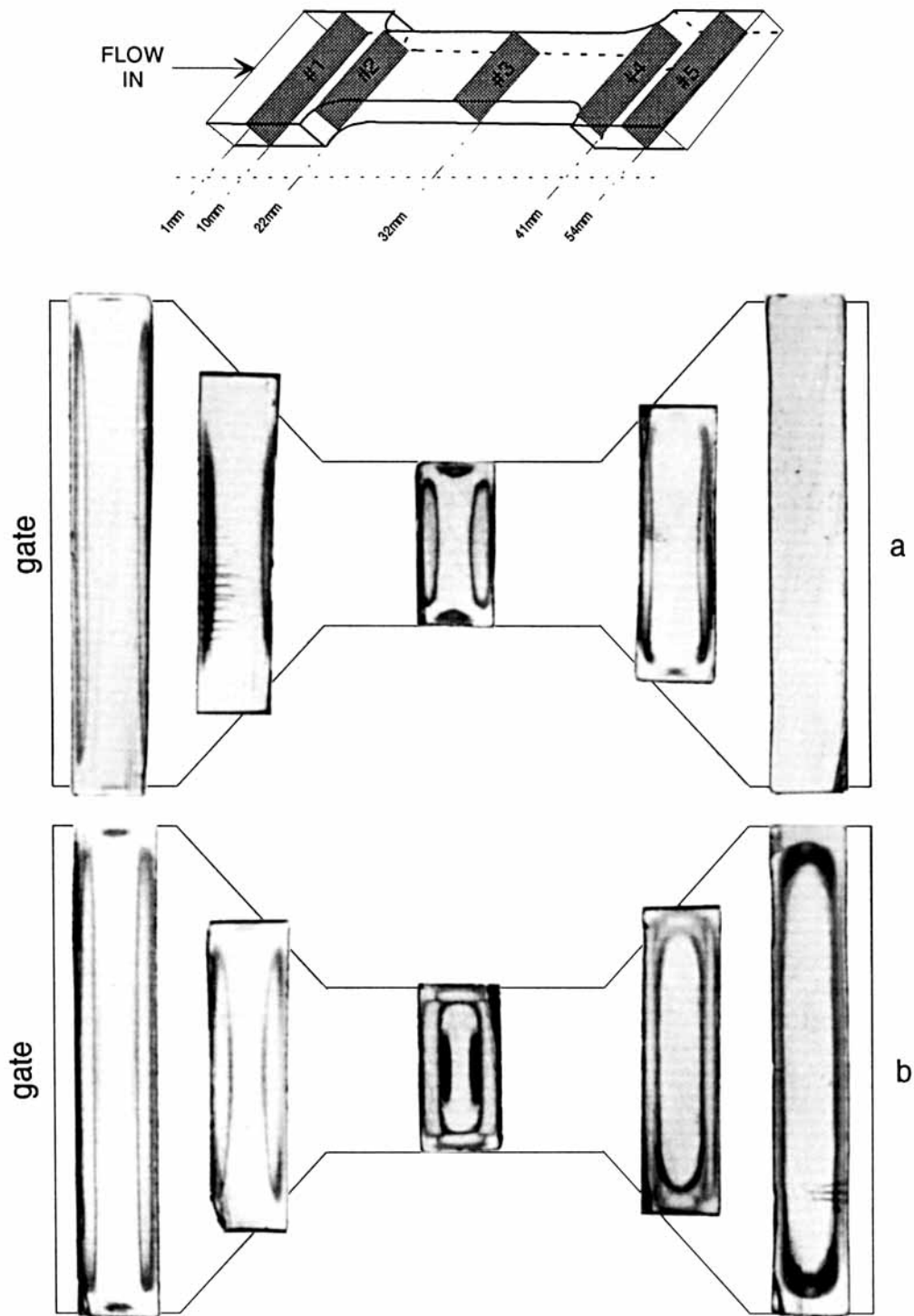
Figure 8   Transmission photomicrographs of the A-cut samples taken from the indicated locations of the samples molded at 40°C. Injection speed is (a) 2.1 cm^3/s; (b) 6.9 cm^3/s; (c) 34.5 cm^3/s.

locations of sPS small dumbbells using procedure B. We can clearly observe a multilayered structure consisting of dark and light layers that evolves with location in the mold, injection speed, and temper-

ature. Although the layer structure of the sPS is similar to the amorphous–crystalline–amorphous (light–dark–light) alternations observed during the injection molding of other slowly crystallizing poly-
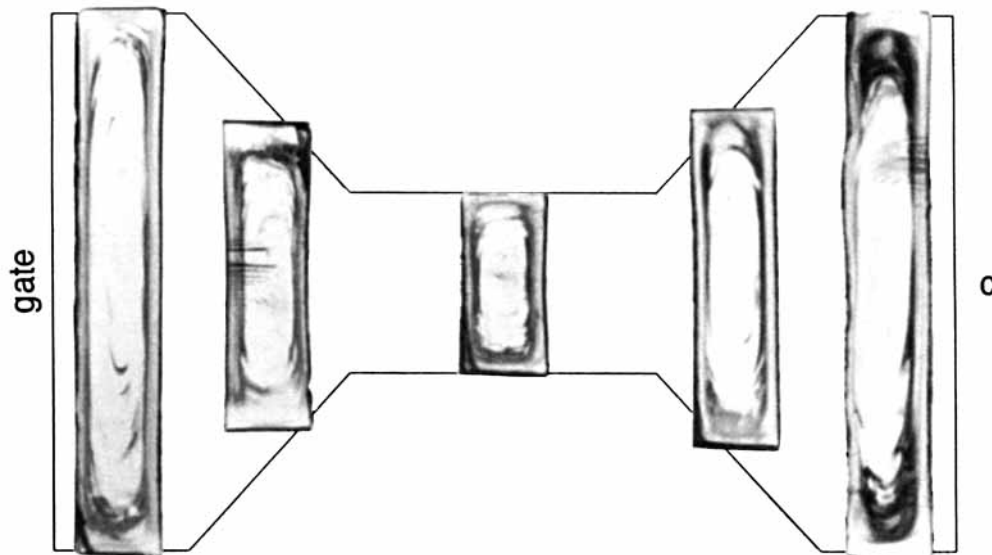
Figure 8 (*Continued from the previous page*)

mers,[34-37] it is more complicated. At 40°C mold temperature, which is below the T_g of sPS (T_g = 90°C), we observe a very thin transparent skin and a transparent core (Fig. 3). The thickness of these layers increases at the locations where the sample is subjected to low stresses; namely, away from the gate at location #1, at the diverging region (location #4), and at the end of the dumbbell (location #5).

Sandwiched between the transparent layers are a dark layer and a translucent layer. Contrary to the transparent layers, the thickness of both the translucent and dark layers increases at the locations subjected to high stresses; namely, at the gate (location #0), converging (location #2), and neck (location #3) regions of the dumbbell. When the mold temperature is increased above the T_g (Figs. 4 and 5), the transparent skin and core layers disappear and the structure of the FD–ND plane consists of the translucent layer near the skin and the dark layer at the interior of the part.[†] Several sublayers are also visible in the interior dark region. The thickness of the translucent layer increases, at the expense of the dark layer, in the regions where polymer chains experience high stresses during molding. However, at a given location the overall thickness of the translucent layer decreases as the mold temperature is increased. Increasing the injection speed causes a decrease in the thickness of both the translucent and the dark layers at low mold temperatures;

whereas at high mold temperatures, only the translucent layer decreases in thickness.

Complex flow patterns reminiscent of melt fracture phenomena can be observed at the divergent and end regions of the small dumbbells. These are shown in Figures 6 and 7, where the samples are used as negatives to reproduce the details of these structures (i.e., the dark and light colors are reversed). In the ND–FD plane (Fig. 6), we can still distinguish an alternating sequence of dark and light layers; however, in this case they are not localized to skin or subskin region but are distributed in the thickness direction and in general follow the stream lines. The C-cuts (Fig. 7) taken from the center of the FD–TD plane (core) were included in order to obtain a three-dimensional visualization of the flow. In this plane we can differentiate the samples molded at lower injection speed from those molded at higher speed. In the former samples, the complex flow patterns are concentrated at the center of the end region, whereas they cover almost the whole width of the latter samples. The structure of the white layers that branch out from skin (refers to TD in this cut as opposed to ND in A and B cuts) are similar to the patterns caused by the well-known fountain flow.[39] On the other hand, at the center of the mold the shape of the layers suggests an instability in the flowing melt stream. Thus the simple mold-filling by fountain flow at the earlier stages transforms into a complex filling at the final stages and is limited to the center of the cavity.

Study of the A-cuts showing the TD–ND plane of the samples (Figs. 8–10) revealed further details

[†] In these photomicrographs the intensity of the light was increased to reveal details of the internal structure; the transparent appearance of the skin layer is an artifact.
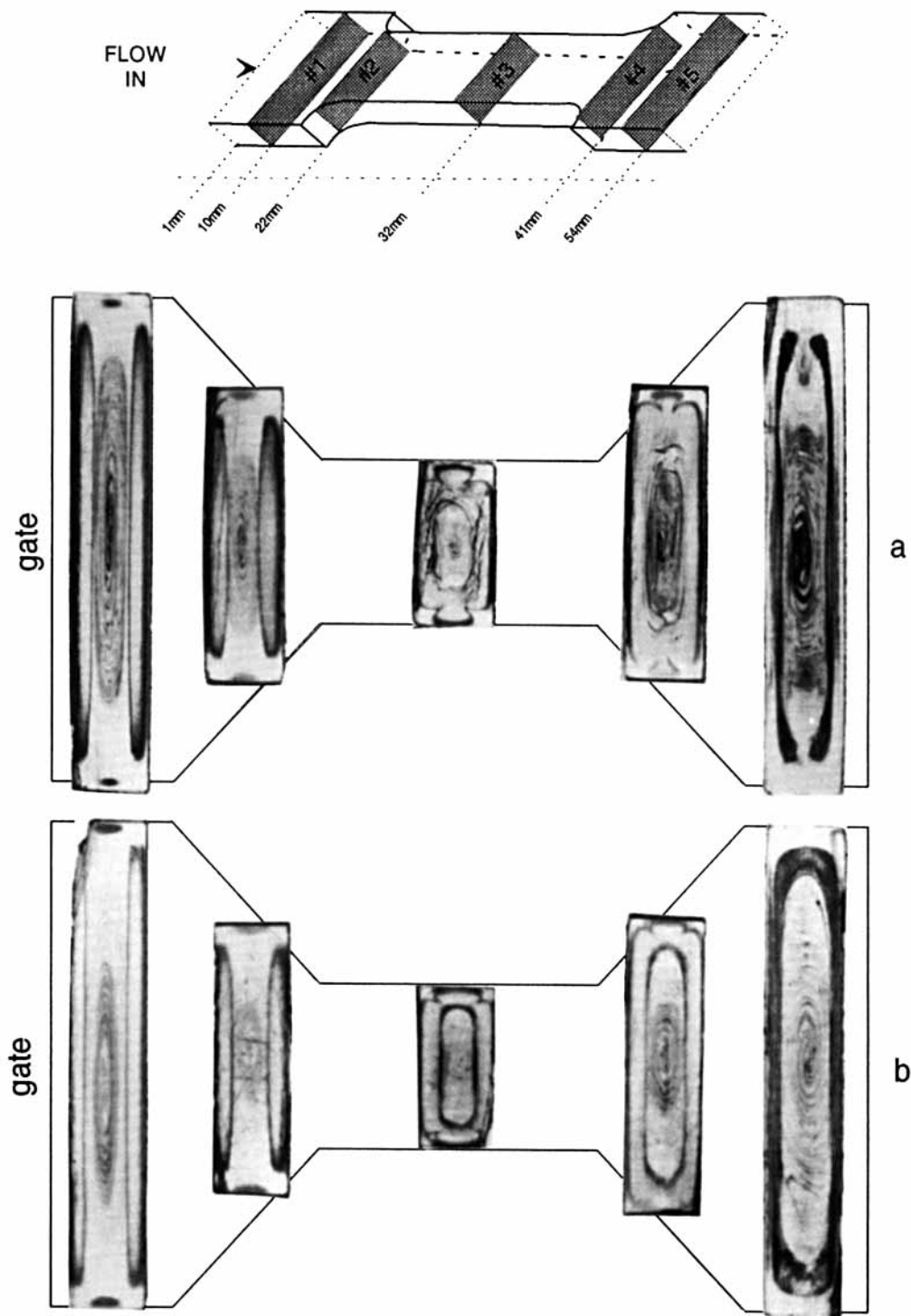
Figure 9 Transmission photomicrographs of the A-cut samples taken from the indicated locations of the samples molded at 110°C. Injection speed is (a) 2.1 cm³/s; (b) 6.9 cm³/s; (c) 34.5 cm³/s.

about the overall morphology of the small dumbbells. In this plane, the translucent layer extends like a strip and covers the majority of the transverse direction next to the skin. At locations where the

polymer chains are subjected to high stresses, this strip extends next to the skin of all four surfaces to form a ring that is interrupted only at the corners (stagnancy points). These strips are thickest at the
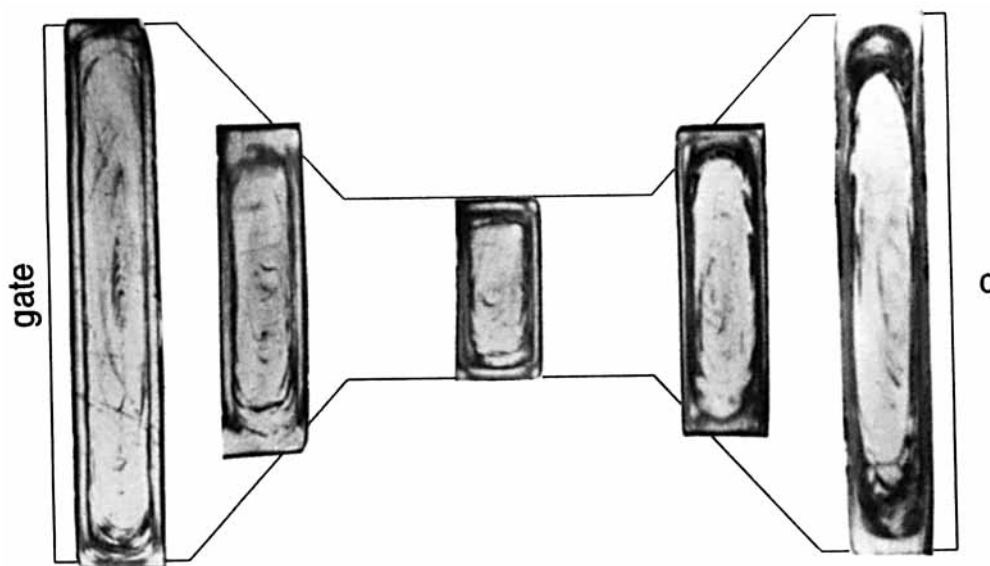
Figure 9   (*Continued from the previous page*)

center of TD and ND planes and their thickness decreases toward the corners. Dark layers circumscribing the translucent strip are also visible in this plane. Note that the dark sublayers observed in the B-cuts taken from locations #0, #1, and #2 of the samples molded at 110 and 140°C are actually sections of ringlike dark layers.

The overall effect of increasing mold temperature is to increase the area covered by dark regions and to decrease the area covered by the translucent strip. The thickness of the latter also becomes more uniform as the mold temperature is increased. Increasing the injection speed mainly affects the translucent layer; its area reduces and its thickness along the flow direction becomes uniform.

We also observed that in the TD–ND plane the complex flow patterns seen in the end region of the samples manifest themselves as spirallike layers that concentrate at the center of the sample. In this plane they are more clearly visible and are not limited to the end region of the sample but extend throughout the mold, especially in the samples molded above the T_g of sPS. The patterns are strongest at the core and end regions of the samples, supporting the fact that the complex flow takes place toward the final stages of the mold filling.

Differential Scanning Calorimetry

Figure 11 shows the DSC scans of the skin (#2a) to core (#2e) C-cuts taken from a small dumbbell molded at 110°C using the high injection speed. The thickness of each slice (a–e) was around 0.18 mm. We observed the T_g around 90°C, the cold crystal-

lization exotherm around 135°C, and the melting endotherm at about 265°C. The DSC spectra of skin layers a and b show another very weak melting endotherm (see arrows in Fig. 11) around 295°C. As the HOT-STAGE MICROSCOPY section shows, this secondary peak is caused by a crystal population having a higher melting point. The absence of the cold crystallization peak near the skin layers indicates that these regions consist of crystalline sPS. The corresponding crystallinity profiles (Fig. 12) show a maximum near the skin where the translucent layers are observed. As the mold temperature increases, the percent crystallinity of the core region increases and the crystallinity profile becomes more uniform. On the other hand, when the injection speed is increased, the maxima becomes sharper and its position shifts closer to the skin. These results indicate that both the translucent and dark layers, observed in the optical photomicrographs, are crystalline. The main difference between these layers is the crystallite sizes. In regions where the polymer chains are subjected to very high stresses during the molding, the sizes are at or smaller than the wavelength range of the visible light, thereby appearing translucent. The darkness of the secondary layers is due, most probably, to the presence of crystallites large enough to scatter light, which leads to partial absorption of the light as it passes through the sample.

Hot-Stage Microscopy

The melting sequence of a microtomed B-cut taken from location #2 of a dumbbell molded at 40°C using
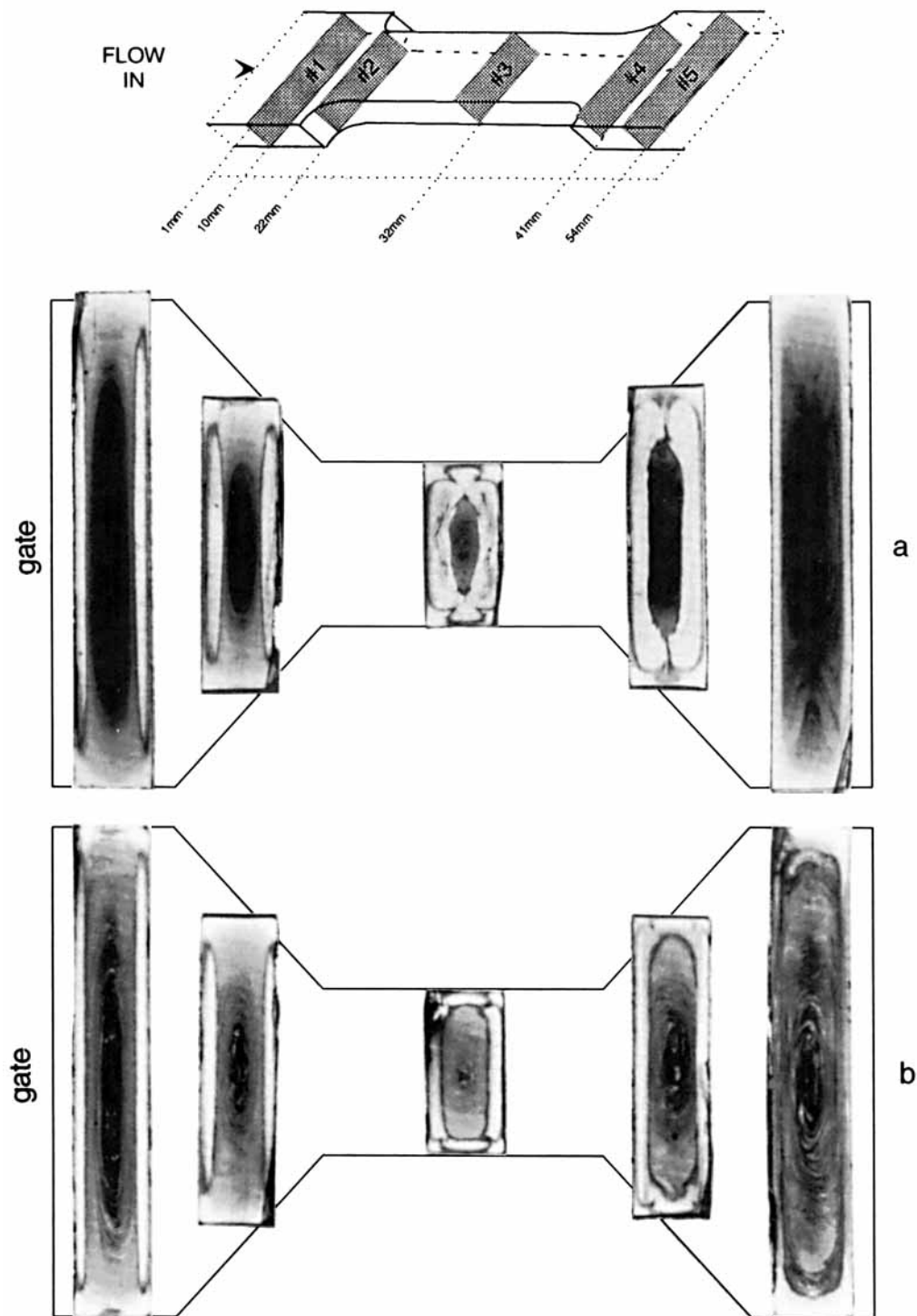
Figure 10 Transmission photomicrographs of the A-cut samples taken from the indicated locations of the samples molded at 140°C. Injection speed is (a) 2.1 cm³/s; (b) 6.9 cm³/s; (c) 34.5 cm³/s.

the medium injection speed is summarized in Figure 13. For this series of experiments the sample cut with Procedure B was placed in the polarized light microscope between the crossed polars with the flow direction making a 45-degree angle with the extinction axis of the polarizer and analyzer. At the beginning of the experiment, we could distinguish the same layer sequence we observed during the optical
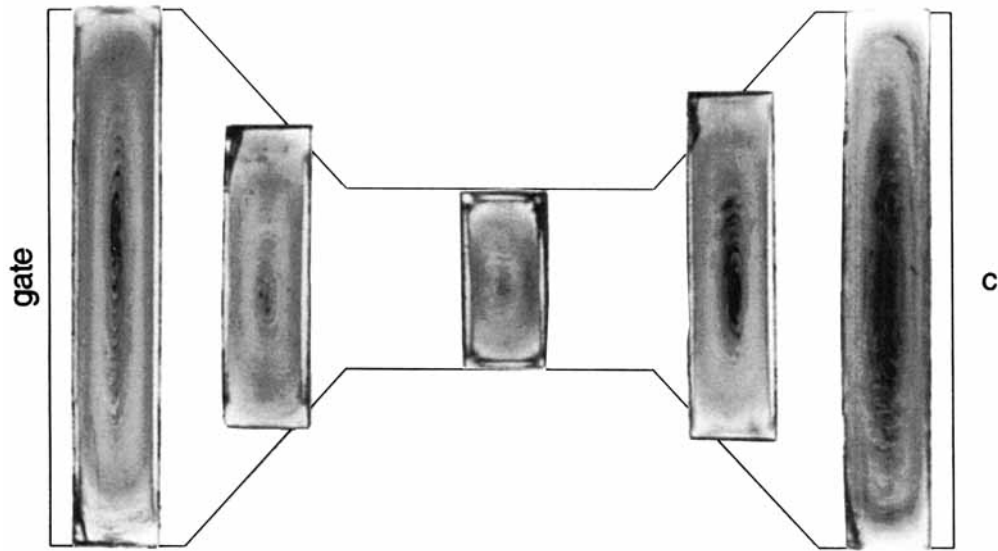
Figure 10 (*Continued from the previous page*)

studies: the amorphous skin, translucent crystalline layer, opaque crystalline layer, and amorphous core. The amorphous core initially exhibited a high intensity. The depolarized light intensity passing through the core and skin gradually decreased at 100°C (around the T_g of sPS) due to relaxation with the onset of segmental motion. The core slowly started to crystallize at around 115°C and this process was completed at around 180°C. During this stage the core of the sample became opaque. We observed no significant morphological change between 180 and 260°C. The melting that started at around 270°C could be observed by an increase in depolarized light intensity of all the layers. At 275°C

the light intensity reached its peak, and the core of the material melted immediately after the peak was reached. Around 290°C the shear-induced crystalline layers near the skin started to melt; the melting proceeded from the core toward the skin. Around 295°C
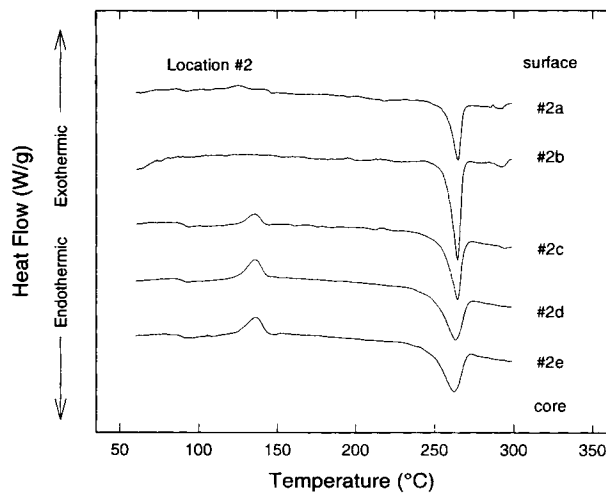

Figure 11 Skin-to-core DSC scans of samples molded at 110°C using the high injection speed. Location #2.
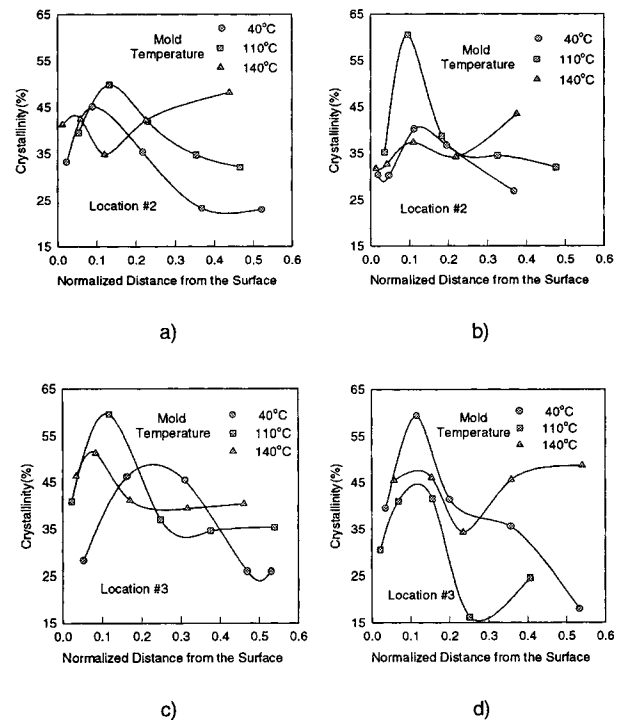
Figure 12 Effect of mold temperature on crystallinity variation along the normal direction of injection molded sPS small dumbbells. Injection speed is: (a) and (c), 6.9 cm³/s; (b) and (d), 34.5 cm³/s.
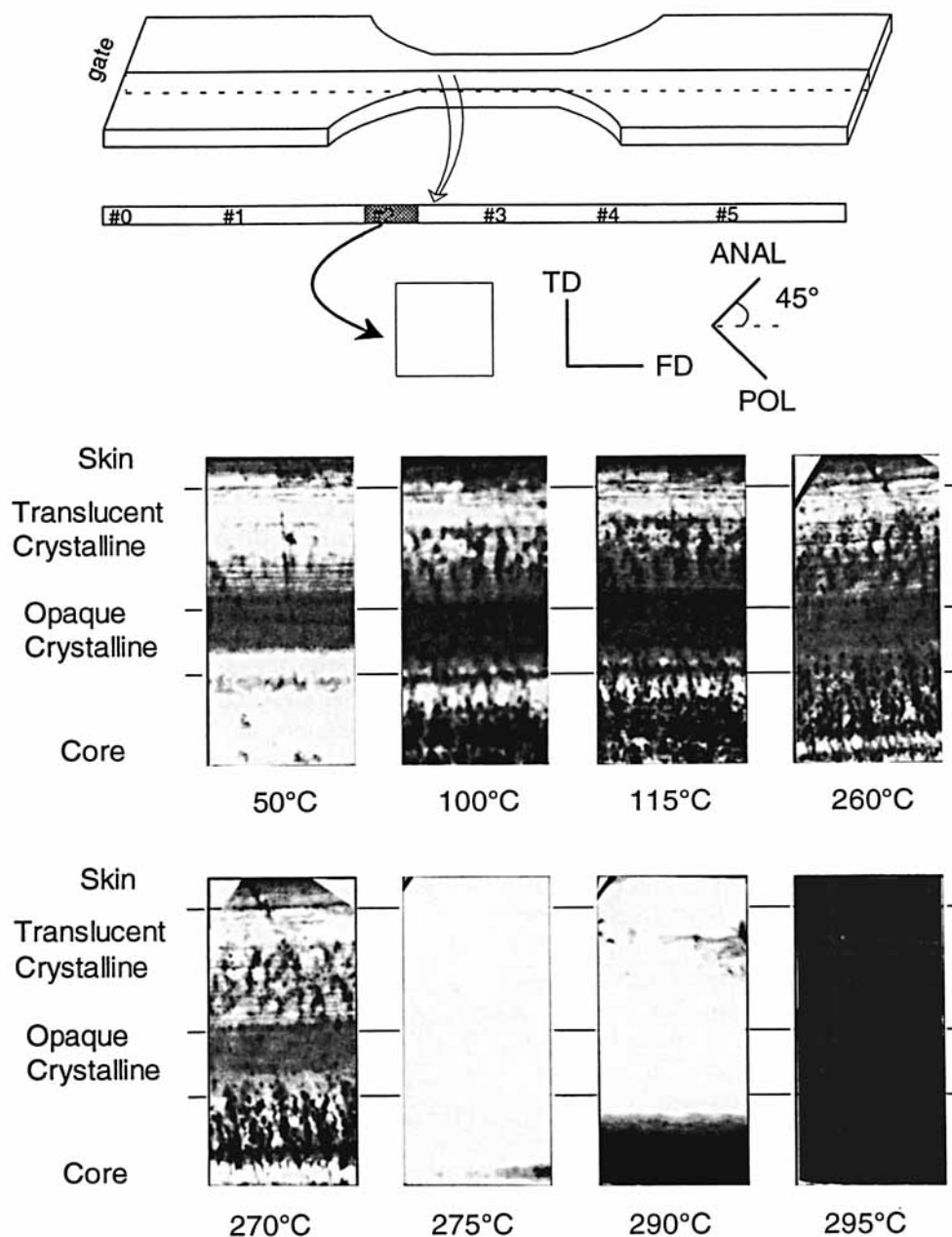
Figure 13 Melting sequence of a sample molded at 40°C using the medium injection speed. Polarized transmission photomicrographs taken from a B-cut placed at 45 degrees to cross-polars.

the bulk of the sample became molten, however thread-like structures could be observed in the translucent crystalline region. The melting was complete at 297°C. Figure 14 shows the details (200×) of the translucent layer morphology. Threadlike structures were observed similar to the structures seen during the melting of shear-crystallized layers in injection-molded PEN.[37] These are most likely extended chain crystals that formed during the flow and have higher melting points.

FTIR

In order to determine the structural differences that lead to the formation of translucent and dark crystalline layers, we first attempted to characterize them through FTIR. The evolution of FTIR spectra going from skin to core of location #2 of this sample is shown in Figure 15. The regions near the skin and core are amorphous, as marked by the absence of crystalline 1222-cm^{-1} (α-form) or 935-cm^{-1} (β-

form) bands. The appearance of a strong 1222-cm^{-1} peak in the spectra taken from the intermediate layers indicates the existence of α-form crystals in these layers. The 935-cm^{-1} band was absent in all the studied samples, eliminating a possible formation of β-form crystals. The intensity and area of the crystalline 1222-cm^{-1} band show significant changes from skin to core, indicating a corresponding change in the crystallinity profile. In order to obtain a semiquantitative description of this change we analyzed the 1250–1100-cm^{-1} region of the samples molded at 40°C and 110°C.[‡] The area under the three characteristic peaks (namely, 1154, 1181, and 1222 cm^{-1}) were determined by peak separation. Figures 16 and 17 summarize the results obtained by normalizing the 1222-cm^{-1} peak using three different procedures: (1) intensity of 1222-cm^{-1} peak/intensity of 1181-cm^{-1} peak; (2) area of 1222-cm^{-1} peak/area of 1153-cm^{-1} peak; and (3) area of 1222-cm^{-1} peak/area of 1187-cm^{-1} peak. We found that normalizing the crystalline peaks by using the integrated areas yielded more consistent results when compared to the intensity normalization procedure suggested by de Candia et al.[31] The relative absorbance profiles are in agreement with the DSC results.

Micro-Beam Wide Angle X-Ray Diffraction

Figure 18 shows a typical wide angle X-ray diffraction (WAXD) pattern of the crystalline sPS taken from injection-molded samples. We could index strong and very highly oriented 110, 300, 220, and 211 planes belonging to the α-form of sPS. The MMBX WAXD patterns taken at a series of locations from skin to core are shown in Figures 19, 20, and 21, along with transmission optical photomicrographs of the same locations in the parts. These WAXS patterns were taken with the X-ray beam along the transverse direction, thus the vertical direction corresponds to the flow direction and the horizontal direction to the normal direction.

Figure 19(a), WAXD patterns of a sample molded at 40°C using the medium injection speed, shows a thin skin layer that has weak but distinct diffraction spots superposed on a weak amorphous halo. This indicates the presence of both the amorphous phase and oriented crystals at the skin. Moving toward

---

‡ Our analysis was limited to the samples molded at 40 and 110°C. As will be shown in the next section, the orientation of c-axis in the direction of flow is quite high in these samples, thus the orientational effects on the strongly parallel 1222-cm^{-1} band can be neglected. On the other hand, the orientation of the samples molded at 140°C varies from skin to core, preventing us from using them for crystallinity measurements.
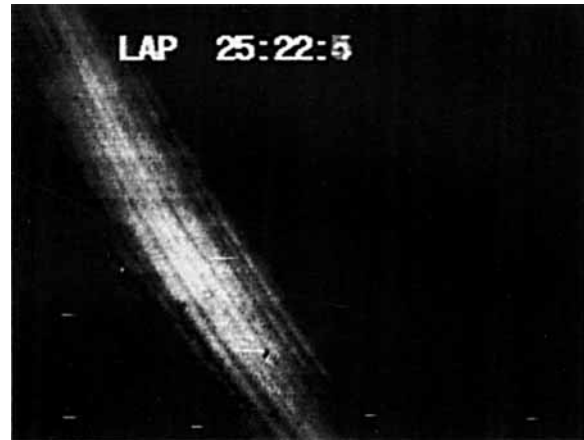

Figure 14 Polarized transmission optical photomicrographs showing the details of the morphology of the translucent layer around 300°C. Sample molded at 40°C using the low injection speed.

the core, the intensity of the diffraction spots increases, indicating that the degree of crystallinity increases in the subskin layers. Moreover, the absence of azimuthal spread of the spots indicates a high level of orientation of the chain axis in the flow direction. Just before the core is an azimuthal broadening of the diffraction spots due to a decrease in this orientation. The core of the sample consists of amorphous sPS characterized by the amorphous halo. When we map the positions of the WAXD patterns onto the optical photomicrographs, we find that the highly crystalline and oriented region corresponds to the translucent layer, the moderately oriented region to the dark layer, and the amorphous region to the transparent core.

Figure 19(b) shows the same sequence for the sample molded using the high injection speed. In this case, although the overall trend is the same, the degree of crystallinity is lower than the former case. The WAXD patterns of the sample molded at 110°C are very similar to those molded at 40°C; however, the overall degree of crystallinity is higher. This is manifested by an increase in the intensity of the diffraction spots and the appearance of weak diffraction rings in the core (Fig. 20). Finally, increasing intensity and azimuthal spread of the WAXD spots indicate that there is a significant decrease in the level of orientation and an increase in overall crystallinity in the small dumbbells molded at 140°C (Fig. 21). The X-ray patterns confirm the results of thermal and FTIR analysis and show clearly that the translucent layers have not only a higher crystallinity but also a higher orientation than the dark
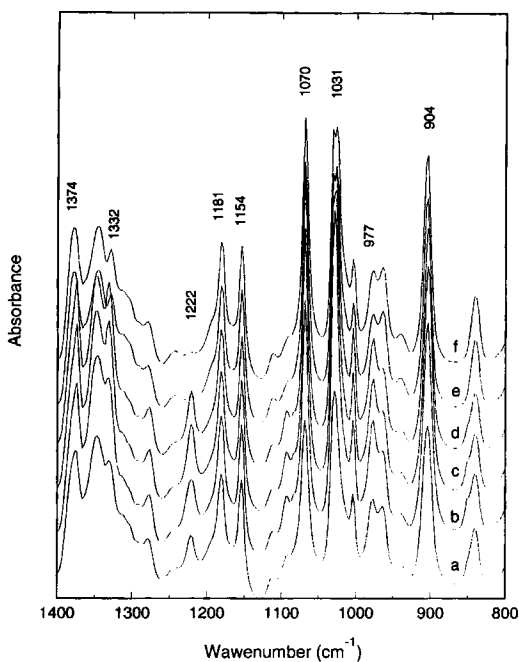
Figure 15 FTIR spectra taken from a sample molded at 40°C using the high injection speed. Location #2. Distance between each scan is 150 μm. (a) Skin; (f) core.

layers that are situated adjacent to the translucent layers toward the core.

Tensile Properties

Including the samples molded at low mold temperatures, injection-molded sPS small dumbbells showed brittle fracture when tested in tension [Fig. 22(a)]. Figures 22(b) and (c) show that both tensile strength and modulus exhibit a maximum at 110°C mold temperature. There is no significant effect of injection speed on mechanical properties; the exception is the sample molded at 40°C and at low injection speed (6.9 cm³/s), which shows the double crystalline layer and higher crystalline orientation at wider regions of the sample.

DISCUSSION

The study of sPS showed that evolution of crystallinity gradients with molding conditions is characteristic of slowly crystallizing polymers.[34-37] The final morphology is a result of a local competition between the time required to cool the polymer to a given temperature and the time required to crystallize the material at that temperature. Another critical factor in this competition is the stress history, since it can change the crystallization kinetics drastically at a given temperature.[40] A convenient way of determining the final stress profile of the molded parts is to measure the birefringence patterns.[41] Figure 23 shows typical birefringence profiles observed in the FD-ND plane of injection-molded polymers. We observed that the profiles have two maxima: one at the skin and another at an intermediate position between the skin and the core. After the second maximum the birefringence gradually decays toward the core. The formation of these patterns was explained by the kinematics of the mold filling and concurrent heat transfer.[42,43] However, the sharpness of the boundary between the stress-induced crystalline layers and the amorphous core suggests that the local (dynamic) stress field is more critical than the final stress field in the formation of the layers. The maximum of the dynamic shear stress should be in the "zone" between the frozen layer and the flowing melt. The location of this maximum and its spread depends on several variables, such as mold geometry, mold temperature, injection speed, and melt temperature. These variables will influence the competition between cooling and crystallization by modifying not only the stress history but also the
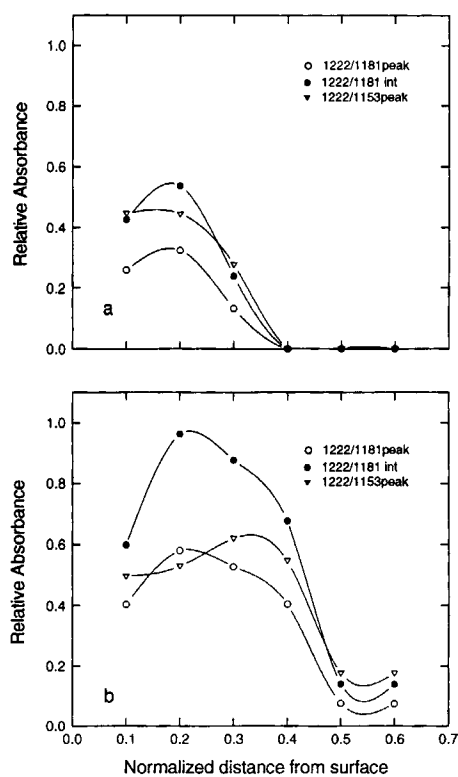

Figure 16 Normalized absorbance of the 1222 cm⁻¹ band as a function of distance from skin. Sample molded at 40°C. Injection speed is (a) 6.9 cm³/s; (b) 34.5 cm³/s.
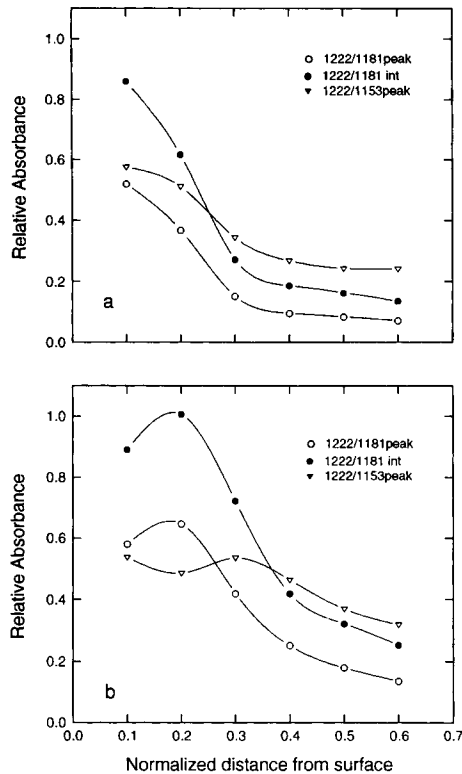
Figure 17 Normalized absorbance of the 1222 cm^{-1} band as a function of distance from skin. Sample molded at 110°C. Injection speed is (a) 6.9 cm^3/s; (b) 34.5 cm^3/s.

thermal history. Their effect on the phase transition can best be represented on time–temperature transition (TTT) curves used in our earlier studies to develop a model to connect the stress effects with crystallization.[34–37] These are shown in Figure 24 for three different gapwise locations in the mold and for different molding conditions. The parabolic curve on the right side of the figure represents the locus of points where crystallization begins (induction envelope) whereas the decreasing curve on the left side of the figure is the cooling curve, showing the change of melt temperature with time. When these two curves meet, the phase transition (crystallization) begins. The effect of applying stress to the polymer is to enhance nucleation and surface area available for growth such that the induction time is reduced and crystallization temperature is increased. On the TTT curve, this corresponds to shifting the induction envelope to higher temperatures and shorter times. Increasing melt or mold temperature, on the other hand, reduces the overall stress history by decreasing the viscosity of the material and increases the cooling time and the rate of relaxation. This moves the TTT curves to longer times, approaching that of quiescent crystallization. Figure

24(a) illustrates the structure formation on the skin (location of first maxima in the birefringence profile) at different mold temperatures. At low temperatures, rapidly increasing frozen-layer thickness narrows the already thin flow channel at locations near the gate where the cooling time is longer. This causes the material to build a high stress history, especially in the converging (location #2) and neck (location #3) regions where the deformation field has an additional elongational component. Such a high stress history improves the crystallization kinetics; however, the cooling rate of the samples molded at 40°C is much too fast for the two curves to meet, causing the formation of the amorphous skin layer. When the cooling rate is lowered by increasing the mold temperature to 110 or 140°C, the cooling and crystallization curves meet even at the skin region, eliminating the amorphous skin layer. The same effect can be observed if we proceed toward the core: the rate of heat transfer is lowered by the poorly conducting skin layers while the stresses persist (second maximum in the birefringence profile); thus the stress-induced crystallization rate overcomes the cooling rate and the two curves intersect [Fig. 24(b)]. These arguments are further supported by the highly oriented WAXS patterns of the stress-induced crystalline layers. Finally, at the core, although the cooling rate is slower, the material has very low stress history (final minimum in the birefringence profile). As a result, the induction envelope is moved to higher crystallization times and lower crystallization temperatures, preventing the two curves from intersecting at 40°C, where the cooling rate is faster than the thermal crystallization
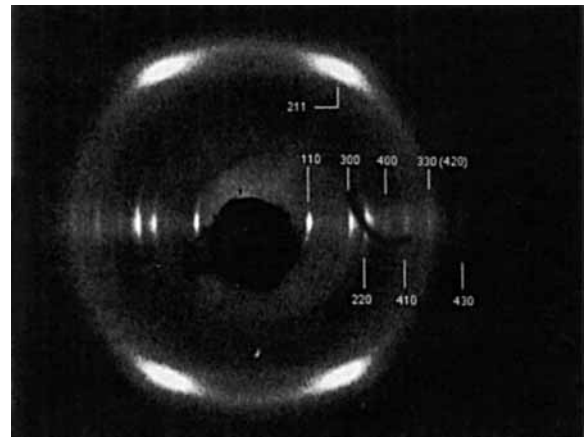

Figure 18 WAXD patterns taken from the crystalline region of a sample molded at 110°C using the medium injection speed. The planes are indexed according to the α-form of sPS.
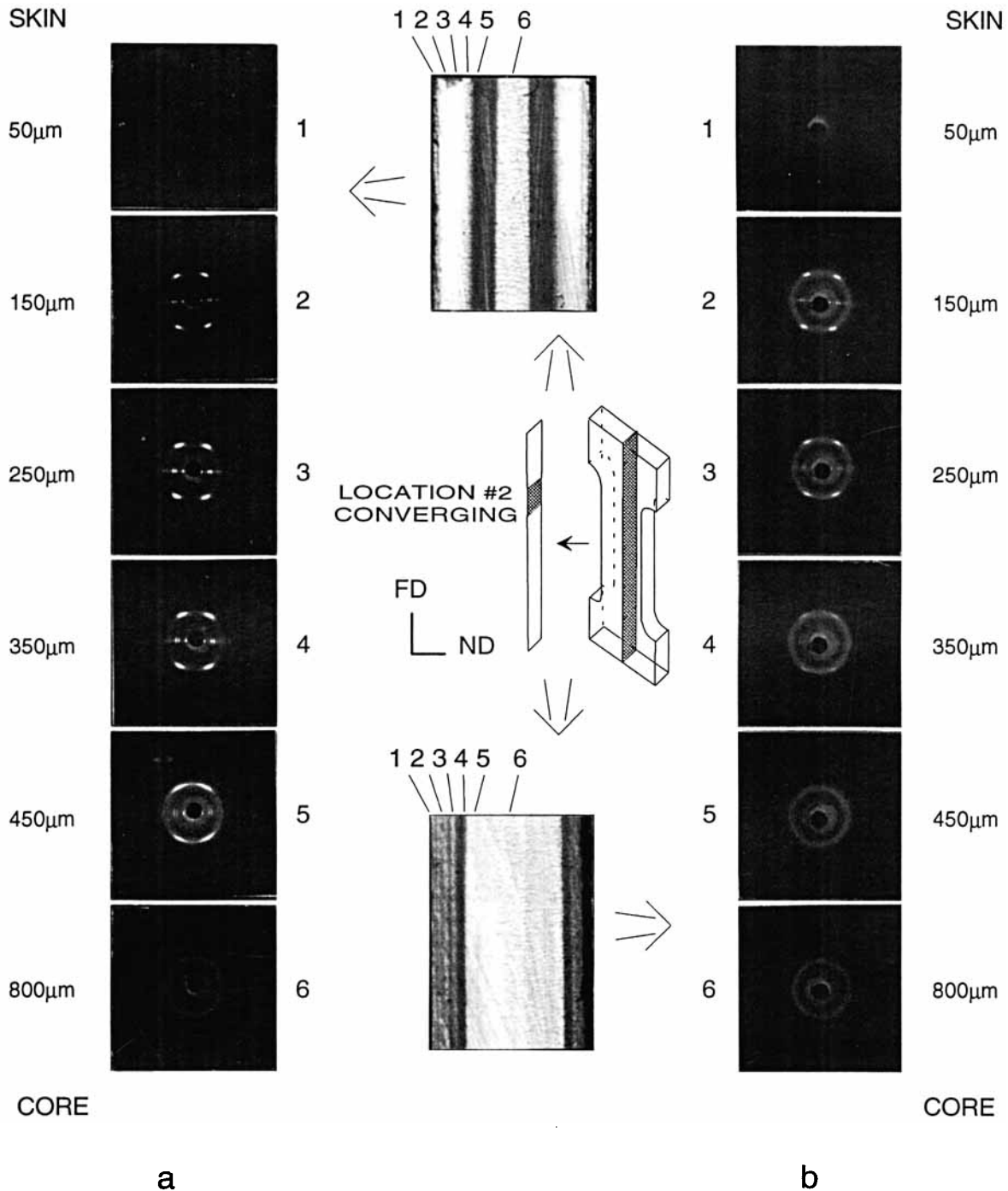
Figure 19   Skin-to-core MMBX WAXD patterns of the sPS taken from location #2 of a sample molded at 40°C. The position of the X-ray beam is indicated on the accompanying transmission optical photomicrograph. Injection speed is (a) 6.9 cm³/s; (b) 34.5 cm³/s.

rate. When the mold temperature is above the T_gs (110 and 140°C), the cooling rate is further slowed, allowing the temperature at the core to remain around the thermal crystallization temperature [Fig. 24(c)]; as a result, the cooling curves intersect the induction envelope, causing the start of crystallization. The

crystals are then formed under quiescent conditions during the holding stage, resulting in the diffraction rings characteristic of randomly oriented crystals.

The effect of mold geometry and injection speed, although not shown in Figure 24, can be explained in a similar fashion. We observed earlier that the
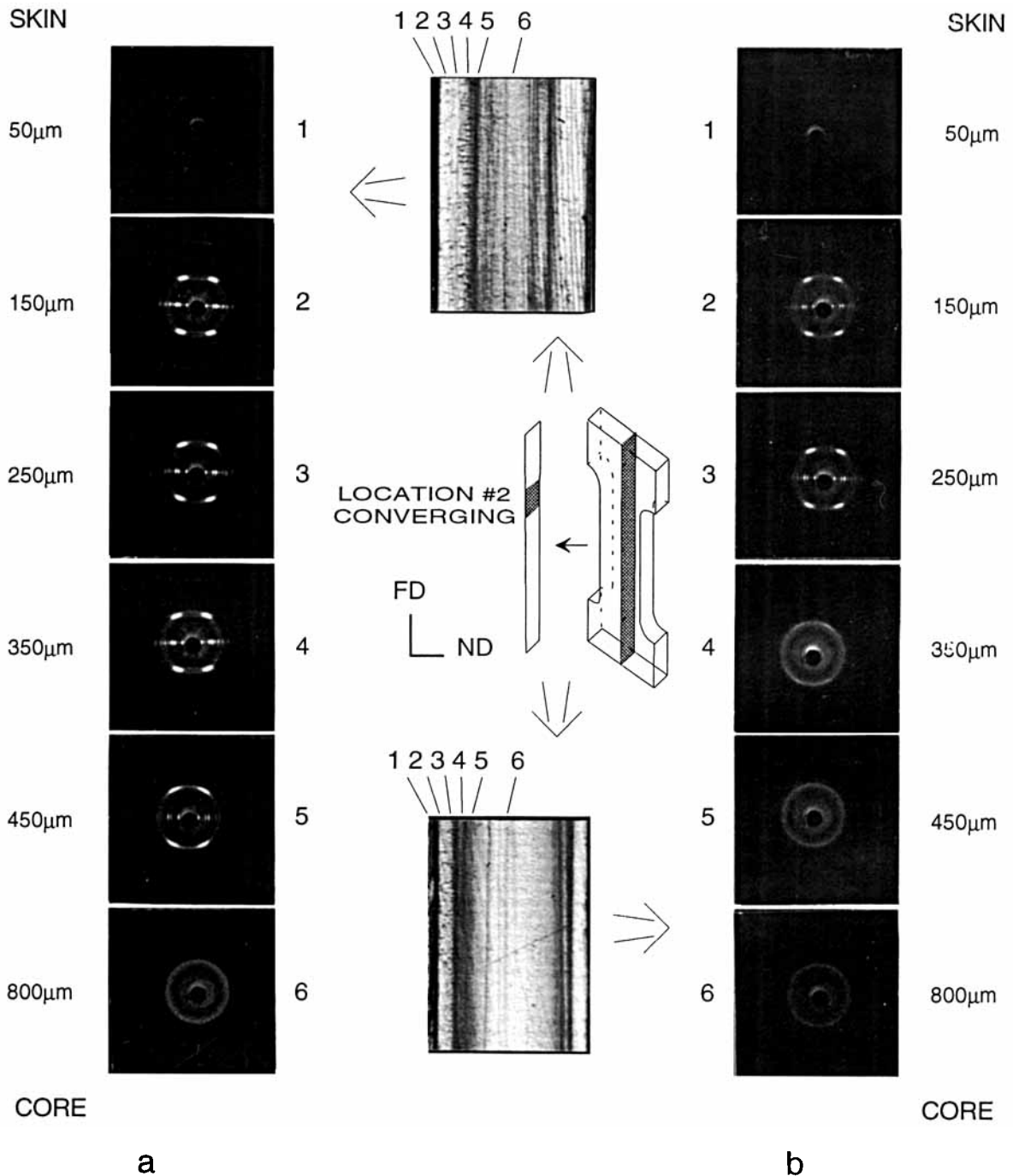
Figure 20   Skin-to-core MMBX WAXD patterns of the sPS taken from location #2 of a sample molded at 110°C. The position of the X-ray beam is indicated on the accompanying transmission optical photomicrograph. Injection speed is (a) 6.9 cm^3/s; (b) 34.5 cm^3/s.

thickness of the stress-induced translucent crystalline layer decreased at the mold locations where the cross-sectional area for the flow is larger. This is due to the fact that under the same cooling conditions (mold temperature) the local stress history will be reduced in these locations, limiting the region where the material can crystallize. The same is true for the injection speed: by increasing the injection speed we reduce the cooling rate and the thickness of the frozen layer. This translates into a wider flow channel and a lower viscosity, reducing the material's stress history.
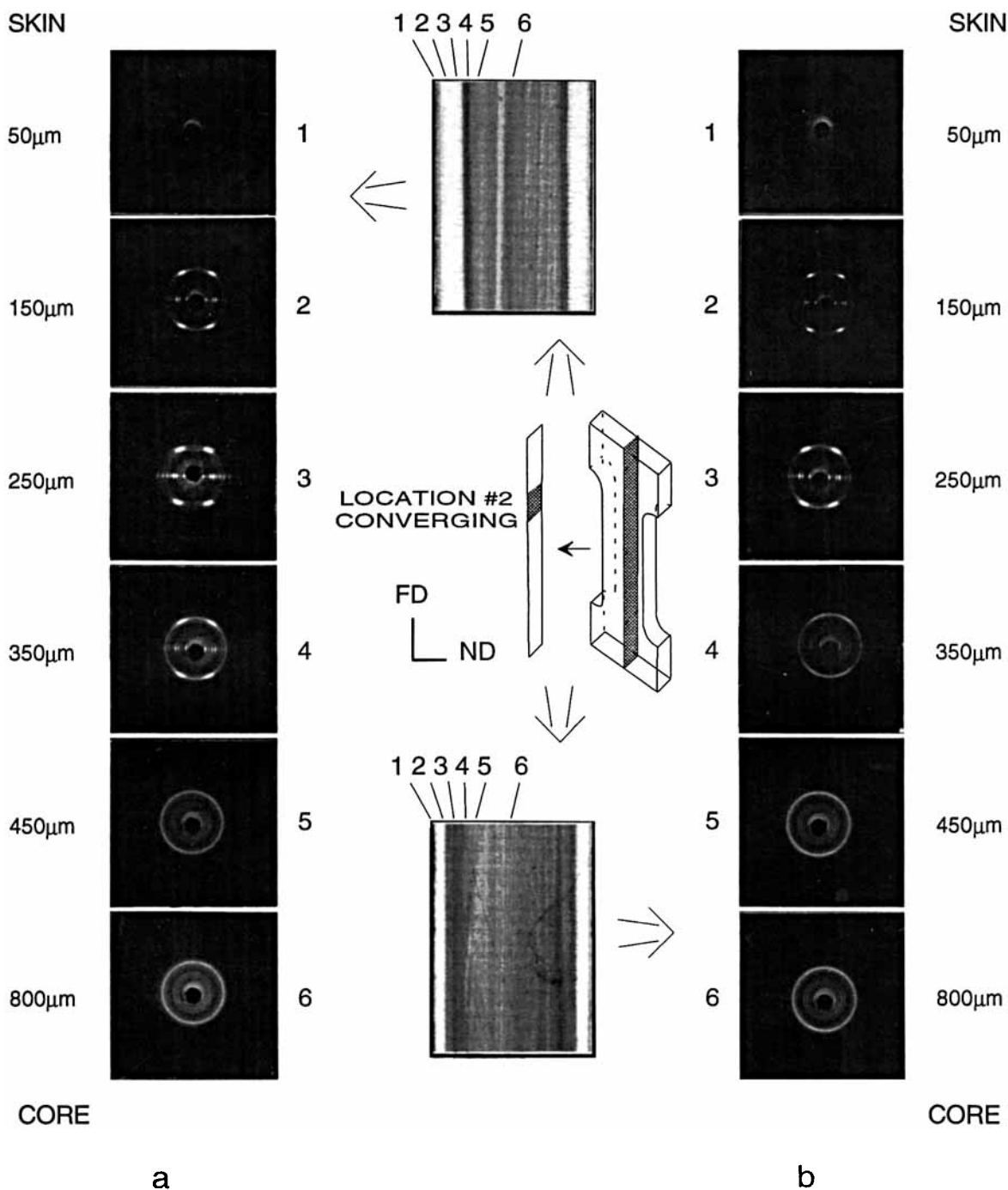
Figure 21   Skin-to-core MMBX WAXD patterns of the sPS taken from location #2 of a sample molded at 140°C. The position of the X-ray beam is indicated on the accompanying transmission optical photomicrograph. Injection speed is (a) 6.9 cm³/s; (b) 34.5 cm³/s.

At this point we can also comment on the formation of dark crystalline layers that surround the translucent layers. Around the second maximum in the birefringence profile, a higher nucleation rate is expected due to the effect of stress. This causes the final size of the crystals to be smaller than the wavelength of the light, making them appear translucent. As we proceed toward the core, the birefringence decays and the stress history as well as the nucleation rate are lower, resulting in the formation of larger crystals whose size is comparable to the wavelength of light. We also must distinguish be-
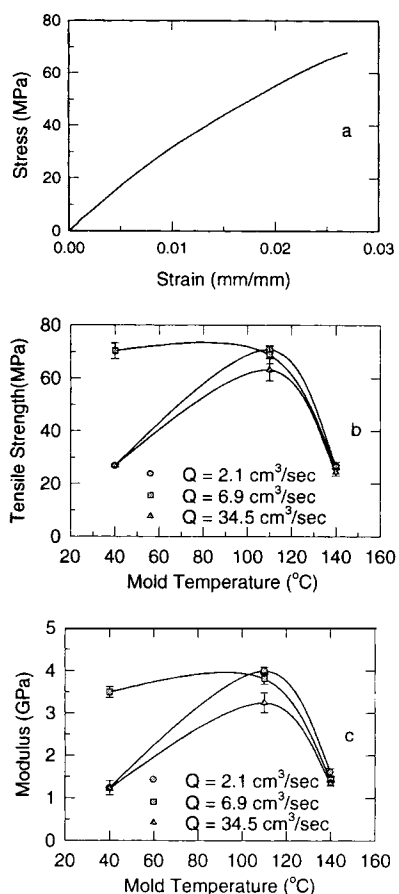
Figure 22   Tensile properties of injection-molded sPS.

tween the dark crystalline layers observed below and above the T_g. The thickness of dark layers in the samples molded at 40°C is significantly affected by injection speed and mold geometry and the layers have a high degree of orientation, suggesting that although their size is larger, they are formed during the filling stage. On the other hand, these variables do not significantly influence the dark layers observed in the samples molded at 110 and 140°C. Moreover, there is a sharp boundary between the stress-induced crystalline layers and the core in the samples molded at 40°C. Also, the WAXS patterns of the dark layers observed at high mold temperatures do not show significant orientation, suggesting that these layers are formed during the holding stage.

The melting experiment clearly showed that the flow-induced crystalline sPS and thermally crystallized sPS have different thermal behaviors. In a previous study,[37] Ulcer and Cakmak observed the same phenomena in injection-molded PEN. However, contrary to sPS, the difference between the melting behavior of thermally and stress-crystallized regions was clearly noticeable in the DSC scans of the PEN

samples. The threadlike precursors that were visible at the final stage of melting and their higher melting point suggest that the stress-induced layers are nucleated by highly extended, bundlelike nuclei. If the final morphology is reminiscent of shish-kebab morphology, where the mass percentage of the higher melting fraction is much lower compared to the crystals that epitaxially grow on them, this would explain the absence of a higher melting peak in the DSC scans.

We believe that the formation of crystalline layers which follow the complex stream lines at the end regions of the samples is related to the elastic memory of the polymer. As the polymer flows in the mold network, it undergoes severe shear stress history that leads to the formation of crystalline "threads" (threadlike shear-induced crystalline nuclei). Due to the elastic memory of the polymer, these threads preserve their stress history even at locations where the stresses are low (i.e., locations #4 and #5). Whenever enough thermal activation energy is provided at some point downstream, they crystallize. And since they follow the local streamlines, they give us the opportunity to delineate the complexity of the flow in this region. These flow patterns resemble the buckling phenomena observed earlier by Hsiung and Cakmak[45] (two of the present authors) in injection-molded liquid crystalline polymers. The buckling was attributed to internal jetting followed by the compression of the innermost stream lines during the packing stage. The existence of periodicity in our samples made us ponder other possible mechanisms related to flow instabilities[46,47,48]: (1) differential orientation between skin and core; (2) failure at critical elastic strain; and (3) propagation and amplification of disturbances by melt elasticity. During injection molding
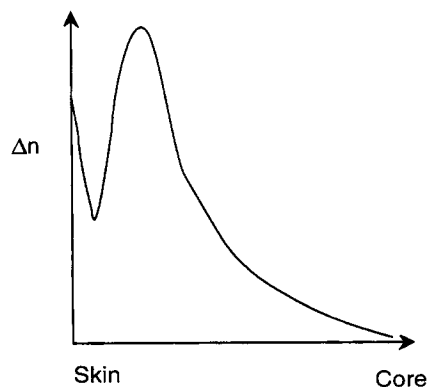

Figure 23   Typical birefringence profiles observed in B-cuts of injection-molded thermoplastics.
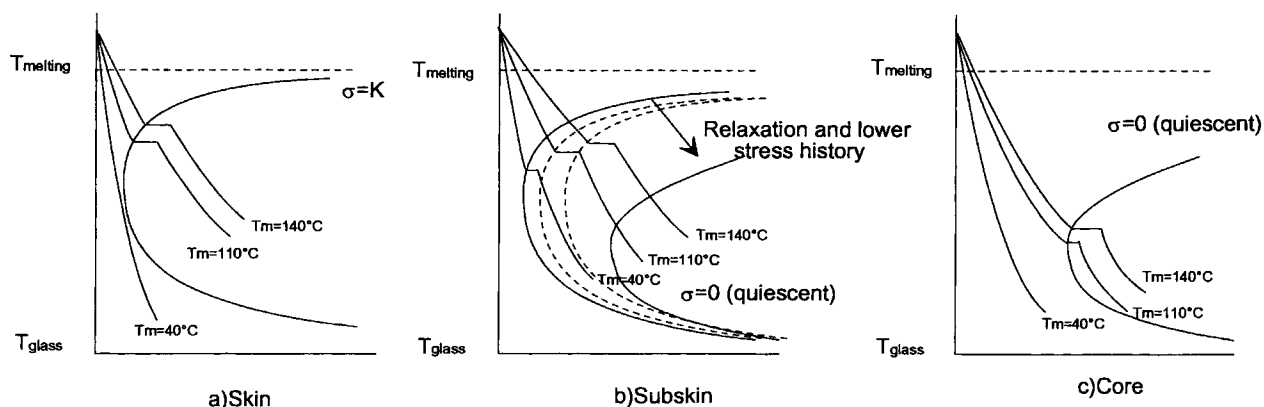
Figure 24 The effect of molding conditions and gapwise position on the shape of TTT curves: (a) skin; (b) shear; (c) core.

through end-gated cavities, the polymer undergoes extensive elongational and shear stress, especially in the gate and the converging region. The intensity of these stresses and related strains increases toward the end of filling due to the reduction of the flow channel by frozen-layer formation. When the material reaches location #1 or location #4 it decelerates substantially because of the increasing cross-sectional area of the flow channel and has the chance of recovering these stresses. It is possible that at this stage a combination of the above mechanisms leads to flow instability. Alternatively, the flow-induced crystallization and nonisothermal effects might contribute to the flow instability by creating a mushy zone. However, at this stage the mechanisms leading to instability cannot be determined without further studies.

Interestingly, the different morphological features seen in the samples molded at different injection speeds did not affect the mechanical properties significantly. The degree of crystallinity and the orientation levels were found to be primary factors determining the tensile strength and modulus of the samples. At lower injection speeds and mold temperatures, preferential orientation of the chains along the flow direction (and thus the tensile testing direction) increases, resulting in improved mechanical properties. As we have seen, the increase of injection speed and mold temperature results in reduction of overall preferential orientation. This is apparently responsible for the reduction of these properties at the highest mold temperature. The samples molded at 110°C showed the best tensile properties, which is attributed to the high crystallinity and orientation of the samples molded at this temperature. The effect of the complex flow patterns

on the mechanical properties was not obvious since they concentrated on the grip region.

CONCLUSIONS

Although it is not a polycondensate, injection-molded sPS showed the amorphous skin–crystalline shear–amorphous core structure observed in other slowly crystallizing polycondensates, such as PEN, PEEK, and PPS.[34-37] As with the other polycondensates, the regions of sPS started to crystallize thermally when the mold temperature was above its T_g. The formation of these structural gradients can be explained by the model proposed by Hsiung, Cakmak and coworkers.[34,44] Our optical and WAXS studies showed that the stress-crystallized layers consist of highly oriented α-form crystals which appear translucent due to high nucleation density. The thermally crystallized layers, on the other hand, consist of randomly oriented α crystals and have a lower nucleation density; as a result, they become opaque. We have found that the stress-induced crystalline regions are nucleated by threadlike nuclei whose melting temperature is above the regular melting point of sPS. The complex flow patterns that we observed point to a possible presence of flow instability, especially at the diverging sections of the thin cavities. Despite the structural gradients observed in the injection-molded small dumbbells, the structure–property relationship was controlled mainly by the degree of crystallinity.

REFERENCES

1. N. Ishihara, T. Seimiya, M. Kuramoro, and M. Uoi, (a) *Macromolecules,* **19,** 2464 (1986); (b) Eur. Pat. Appl. 2106d15 (1987).
2. C. Pellecchia, P. Longo, A. Grassi, P. Ammendola, and A. Zambelli, *Makromol. Chem. Rapid Commun.,* **8,** 277 (1987).
3. *Plast. Technol.,* **Feb.,** 26 (1993).
4. Y. Chatani, Y. Fuji, Y. Shimane, and T. Ijitsu, *Polym. Preprints Japan (Eng. Ed.),* **37,** E428 (1988).
5. O. Greis, T. Asano, J. Xu, and J. Petermann, *J. Z. Kristallogr.,* **182,** 52 (1988).
6. O. Greis, Y. Xu, T. Asano, and J. Peterman, *Polymer,* **30,** 590 (1989).
7. A. Immirzi, F. de Candia, P. Iannelli, A. Zambelli, and V. Vittoria, *Makromol. Chem. Rapid. Commun.,* **9,** 761, 765 (1988).
8. V. Vittoria, R. Russo, and F. de Candia, *J. Macromol. Sci., Phys.,* **B28,** 419 (1989).
9. G. Guerra, V. M. Vitagliano, C. de Rosa, V. Petraccone, and P. Corradini, *Macromolecules,* **23,** 1539 (1990).
10. F. de Candia, A. R. Filho, and V. Vittoria, *Makromol. Chem. Rapid Commun.,* **12,** 295 (1991).
11. F. de Candia, R. Russo, and V. Vittoria, *Polym. Comm.,* **32,** 306 (1991).
12. Z. Sun, R. J. Morgan, and D. N. Lewis, *Polymer,* **33,** 660 (1992).
13. V. Vittoria, A. R. Filho, and F. de Candia, *J. Macromol. Sci., Phys.,* **B31,** 133 (1992).
14. Y. Chatani, Y. Shimane, Y. Inoue, T. Inagaki, T. Ishioka, T. Ijitsu, and T. Yukinari, *Polymer,* **33,** 488 (1992).
15. C. de Rosa, M. Rapacciuolo, G. Guerra, V. Petraccone, and P. Corradini, *Polymer,* **33,** 1423 (1992).
16. D. Capitani, C. de Rosa, A. Ferrando, A. Grassi, and A. L. Segre, *Macromolecules,* **25,** 3874 (1992).
17. F. Auriemma, V. Petraccone, F. dal Poggetto, C. de Rosa, G. Guerra, C. Manfredi, and P. Corradini, *Macromolecules,* **26,** 3772 (1993).
18. V. Petraccone, F. Auriemma, F. dal Poggetto, C. de Rosa, G. Guerra, and P. Corradini, *Macromol. Chem.,* **194,** 1335 (1993).
19. Y. Chatani, Y. Shimane, T. Ijitsu, and T. Yukinari, *Polymer,* **34,** 1625 (1993).
20. N. M. Reynolds and S. L. Hsu, *Macromolecules,* **23,** 3463 (1990).
21. R. A. Nyquist, C. L. Putzig, M. A. Leugers, R. D. McLachlan, and B. Thill, *Appl. Spectrosc.,* **46,** 981 (1992).
22. N. M. Reynolds, H. D. Stidham, and S. L. Hsu, *Macromolecules,* **24,** 3662 (1991).
23. R. A. Nyquist, *Appl. Spectrosc.,* **43,** 440 (1989).
24. N. M. Reynolds, J. D. Savage, and S. L. Hsu, *Macromolecules,* **22,** 2867 (1989).
25. M. Kobayashi, T. Nakaoki, and N. Ishihara, *Macromolecules,* **23,** 78 (1990).
26. J. Arnauts and H. Berghmans, *Polym. Comm.,* **31,** 343 (1990).
27. G. Gianotti and A. Valvassori, *Polymer,* **31,** 473 (1990).
28. N. V. Gvozdic and D. J. Meier, *Polym. Comm.,* **32,** 183, 493 (1991).
29. R. D. Wesson, *SPE ANTEC,* **36,** 574 (1990).
30. S. Cimmino, E. di Pace, E. Martuscelli, and C. Silvestre, *Polymer,* **32,** 1080 (1991).
31. F. de Candia, A. R. Filho, and V. Vittoria, *Coll. Polym. Sci.,* **269,** 650 (1991).
32. F. de Candia, G. Romano, R. Russo, and V. Vittoria, *Coll. Polym. Sci.,* **268,** 720 (1990).
33. C. M. Hsiung and M. Cakmak, *Int. Polym. Proc.,* **7**(1), 51 (1992).
34. C. M. Hsiung, M. Cakmak, and J. L. White, *Int. Polym. Proc.,* **5**(2), 109 (1990).
35. C. M. Hsiung, M. Cakmak, and J. L. White, *Polym. Eng. Sci.,* **30**(16), 967 (1990).
36. C. M. Hsiung and M. Cakmak, *J. Appl. Polym. Sci.,* **47,** 125, 149 (1993).
37. Y. Ulcer and M. Cakmak, *Polymer,* **35**(26), 5651 (1994).
38. K. Keuchel, Master's Thesis, University of Akron (1994).
39. L. R. Schmidt, *Polym. Eng. Sci.,* **14**(11), 797 (1974).
40. R. R. Lagasse and B. Maxwell, *Polym. Eng. Sci.,* **16,** 189 (1976).
41. J. L. S. Wales, J. Van Leeuwen, and R. Van der Vijgh, *Polym. Eng. Sci.,* **12**(5), 358 (1972).
42. Z. Tadmor, *J. Appl. Polym. Sci.,* **18,** 1753 (1974).
43. (a) H. Janeschitz-Kriegl, *Rheol. Acta,* **16,** 327 (1977); (b) *ibid,* **18,** 693 (1979).
44. C. M. Hsiung and M. Cakmak, *Polym. Eng. Sci.,* **31**(19), 1372 (1992).
45. C. M. Hsiung and M. Cakmak, *Int. Polym. Proc.,* **VIII**(3), 255 (1993).
46. J. L. White and J. Kondo, *J. Non-Newt. Fluid Mech.,* **3,** 41 (1977/78).
47. S. A. White, A. D. Gotsis, and D. G. Baird, *J. Non-Newt. Fluid. Mech.,* **24,** 121 (1987).
48. K. E. P. Adewale, Ph.D. Dissertation, College of Polymer Science and Polymer Engineering, University of Akron, 1995.